Check for updates

High Power Laser Science and Engineering, (2024), Vol. 12, e43, 8 pages.
doi:10.1017/hpl.2024.24

HIGH POWER LASER SCIENCE AND ENGINEERING

RESEARCH ARTICLE

Compression and acceleration processes of spherical shells in gold cones

Huigang Wei[1,5], Dawei Yuan[1,5,10], Shaojun Wang[2], Ye Cui[3], Xiaohu Yang[3,5], Yanyun Ma[3,5], Zhe Zhang[2,5], Xiaohui Yuan[4,5], Jiayong Zhong[5,6,10], Neng Hua[7], Yutong Li[2,5,8], Jianqiang Zhu[7], Gang Zhao[1,9], and Jie Zhang[2,4,5]

[1] *Key Laboratory of Optical Astronomy, National Astronomical Observatories, Chinese Academy of Sciences, Beijing, China*

[2] *Beijing National Laboratory for Condensed Matter Physics, Institute of Physics, Chinese Academy of Sciences, Beijing, China*

[3] *Department of Nuclear Science and Technology, National University of Defense Technology, Changsha, China*

[4] *Key Laboratory for Laser Plasmas (MOE) and School of Physics and Astronomy, Shanghai Jiao Tong University, Shanghai, China*

[5] *Collaborative Innovation Center of IFSA (CICIFSA), Shanghai Jiao Tong University, Shanghai, China*

[6] *Department of Astronomy, Beijing Normal University, Beijing, China*

[7] *National Laboratory on High Power Laser and Physics, Chinese Academy of Sciences, Shanghai, China*

[8] *School of Physical Sciences, University of Chinese Academy of Sciences, Beijing, China*

[9] *School of Astronomy and Space Science, University of Chinese Academy of Sciences, Beijing, China*

[10] *Institute of Frontiers in Astronomy and Astrophysics of Beijing Normal University, Beijing, China*

(Received 13 March 2024; revised 12 April 2024; accepted 23 April 2024)

Abstract

Double-cone ignition [Zhang *et al.*, Phil. Trans. R. Soc. A 378, 20200015 (2020)] was proposed recently as a novel path for direct-drive inertial confinement fusion using high-power lasers. In this scheme, plasma jets with both high density and high velocity are required for collisions. Here we report preliminary experimental results obtained at the Shenguang-II upgrade laser facility, employing a CHCl shell in a gold cone irradiated with a two-ramp laser pulse. The CHCl shell was pre-compressed by the first laser ramp to a density of 3.75 g/cm^3 along the isentropic path. Subsequently, the target was further compressed and accelerated by the second laser ramp in the cone. According to the simulations, the plasma jet reached a density of up to 15 g/cm^3, while measurements indicated a velocity of 126.8 ± 17.1 km/s. The good agreements between experimental data and simulations are documented.

Keywords: compression and burn; double-cone ignition; laser–plasma interaction

1. Introduction

Significant progress has been made in both direct-drive[1,2] and indirect-drive[3–5] inertial confinement fusion (ICF), while large challenges[6] still exist. Hence alternative paths, such as shock ignition[7], fast ignition[8] and magneto-inertial fusion[9], are being explored. A novel ignition scheme, double-cone ignition (DCI)[10], was recently proposed. Two fuel shells in two head-on gold cones are ablated by focused laser beams to compress the fuel up to 200 g/cm^3 and then accelerate it to a velocity of more than 200 km/s. The pre-compressed plasma jets from the two cones collide to convert the kinetic energies to internal energy in the colliding plasma with higher density for fast ignition by fast electrons. Details of the discussions on these four processes can be found in the above paper.

In this paper, we mainly focus on the first two processes[10], namely compression and acceleration. The first process aims to pre-compress the shell to a high density before imploding the two shells with high velocities. To achieve this goal, multiple shocks are designed to precisely compress the target shell adiabatically, along the quasi-isentropic line. (However, the isentropic compression here is very short compared

Correspondence to: Y. Li, Beijing National Laboratory for Condensed Matter Physics, Institute of Physics, Chinese Academy of Sciences, Beijing 100190, China. Email: ytli@iphy.ac.cn; J. Zhang, Key Laboratory for Laser Plasmas (MOE) and School of Physics and Astronomy, Shanghai Jiao Tong University, Shanghai 200240, China. Email: jzhang1@sjtu.edu.cn

© The Author(s), 2024. Published by Cambridge University Press in association with Chinese Laser Press. This is an Open Access article, distributed under the terms of the Creative Commons Attribution licence (https://creativecommons.org/licenses/by/4.0), which permits unrestricted re-use, distribution and reproduction, provided the original article is properly cited.

https://doi.org/10.1017/hpl.2024.24 Published online by Cambridge University Press

with the common isentropic process and is similar to shock compression. Thus we also use the shock compression to qualify this process.) This would significantly reduce the laser energy needed for implosion. The shocks finally coalesce at the rear surface of the shell, and the accurately timed coalescence of shocks is vital for a high-quality compression. Previous experiments[11,12] were conducted on shock tuning at the National Ignition Facility (NIF) and the compression of fuel was increased by a factor of 3 by finely tuning the arrival time of different shocks when compared to the previous untuned results. For DCI, the second process is to accelerate the target to a high velocity after compressing it to high density. Thus, the laser pulse must be specially designed to achieve this goal.

Here we report the progress of shock experiments performed at the Shenguang II upgrade (SGII-U) laser facility[13]. The initial steps were aimed at studying the compression and acceleration of the outgoing jet in a single cone. It was a proof-of-principle experiment to confirm the feasibility of the first two processes for the DCI scheme. Future experiments will be performed with hundreds of kJ laser energy and double cones. In the present experiment, convergent compression waves generated by the two-ramp laser pulse were employed to compress the spherical CHCl shell. The laser pulse with two ramps was optimized for the CHCl shells in the gold cones to generate jets with both high density and high velocity. As a preparation experiment, a two-ramp pulse, which will ultimately be optimized to a real isentropic laser pulse in future experiments, with a small slope in the first ramp was used to launch a quasi-isentropic compression on the target. This design aims to ensure that the shell follows the isentropic compression, achieving the highest accessible density before being propelled to the highest accessible velocity. The energy distribution in the two ramps of the pulse was carefully designed to achieve this objective. The experiments conducted here are used to investigate the properties of the generated plasma jets from the cones. Optical diagnostics were used to measure the shock velocity in the CHCl shells, and the experimental results were carefully compared with 2D simulations. This is the first of a series of shock experiments for DCI campaigns.

2. Experimental setup

The SGII-U laser facility, which can operate eight beams with 1500 J each at a wavelength of 351 nm, was employed to perform the experiment. The energy balance of the laser beams is less than 10%. Figure 1 represents the schematic experimental setup. The profile of each laser beam was temporally shaped into a two-ramp pulse, as shown in Figure 1. The first ramp pulse started with a step and had a rise time of 2.5 ns, intended to generate a fluid phase behind the shock in the CH shell and subsequently compress the shell along the isentropic path. The second ramp pulse, with a rise time of 2 ns and a maximum intensity 140 times greater than that of the first pulse, was used to further compress and accelerate the target. The laser beams were focused to a spot with a 2 mm diameter flat top profile using a continuous phase plate (CPP). For comparison, some shots with a rectangle pulse were also conducted.

As the initial step for the DCI scheme, the plasma jets at the cone tips should be carefully characterized before collisions; hence only one cone with a shell target was used. Cl-doped polystyrene (CH) was chosen as the shell to

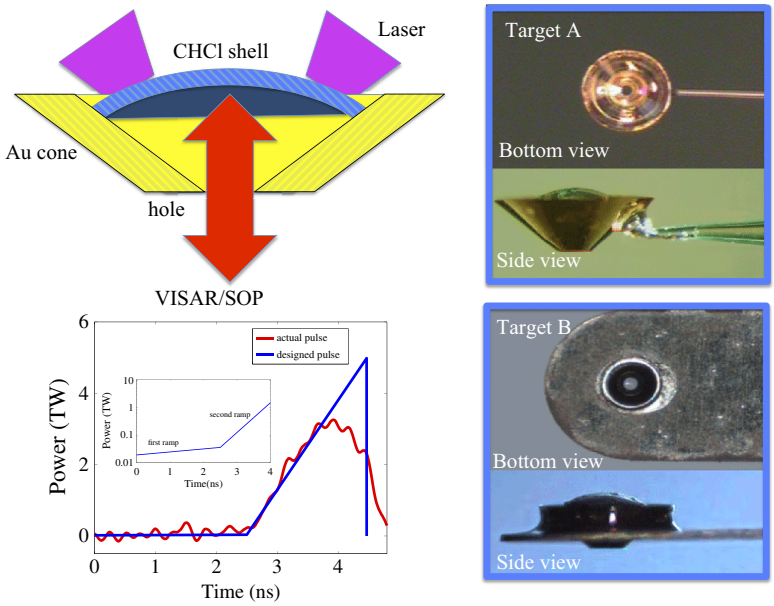


Figure 1. Sketch of the experimental setup with the two-ramp pulse profile and the targets. Four laser beams irradiate the CHCl shell targets. A probe laser penetrates the hole of the Au cone and is reflected back by the shock into the VISAR diagnostics. The target self-emissions are measured by SOP.

https://doi.org/10.1017/hpl.2024.24 Published online by Cambridge University Press

improve the direct-drive implosion performance[14]; meanwhile, chlorine was used as a trace element for other diagnostics. Helium-like triplets from Cl were measured by an X-ray spectrometer and used to determine the plasma densities and temperatures[15]. The shell was shaped into a spherical cap with a cap angle of 50° and a sphere inner radius of 250 μm, which was glued to the wall of the gold cone. The shell was irradiated by four laser beams with intensities up to 4.6×10^{15} W/cm^2. The thickness of the shell was 50 μm. The experimental setup is presented in Figure 1, where the cone was glued to a thin glass pole (Target A) or supported by an Al plate with a hole (Target B). To avoid blocking the instruments to diagnose the jet, type-A targets were used, otherwise type-B targets were used as type-A targets were prone to damage. The shocks generated in the shell strengthen with increased laser intensity. Consequently, the latter shocks propagate faster than the former ones and coalescence at the rear surface of the CHCl shell with the first shock. The CHCl plasma is propelled forward and out of the gold cone through the hole at the tip of the cone. As the CHCl plasma moves forward, it undergoes further compression by the wall of the gold cone.

The shock velocity propagated in the CHCl shell was measured through the hole of the gold cone by the velocity interferometry system for any reflector (VISAR)[16], which utilizes a 50 ns pulse-width probe laser[17]. A 15 mm etalon was used, corresponding to a velocity sensitivity of 4.288 km/s per fringe. An optical fiducial was added to the streak camera to provide absolute timing. The CHCl target has a low reflection for the VISAR probe at 660 nm, and no signal is detected from the CHCl shell through the cone hole before the main laser ablation. The reflector in this experiment is the shock front in the CHCl shell, which can be considered as the beginning of the laser pulse since the shocks are formed rapidly when the laser ablates the CHCl shell. A streaked optical pyrometer (SOP) was employed as a complementary diagnostic to measure the emission of shocks in the CHCl shell.

3. Experimental results and simulations

Figure 2 shows the measured VISAR images for a typical rectangle pulse shot (Figure 2(b)) together with the results for a two-ramp pulse shot (Figure 2(c)). The horizontal direction of these images corresponds to the spatial direction transverse to the shock velocity, while time increases from top to bottom. Figure 2(a) shows the reference image for Target A without the main laser pulses, where only the bright fringes of the VISAR laser beam reflected by the wall surface at the tip of the gold cone can be detected. The fringes corresponding to the stationary CHCl shell were too weak to be detected since most of the VISAR laser passes through the CHCl shell. The laser energy for rectangle pulse was 5.6 kJ with a pulse duration of 2 ns. Simulations showed that a pulse of 2 ns is a preferable choice, which can drive the jet to eject from the tip of the cone near the end of the laser pulse. This can efficiently convert the laser energy to jet kinetic energy for a rectangle pulse. Due to the malfunction of the laser cooling system during the experiments, a relatively stronger pre-pulse was observed before the main pulse. This pre-pulse irradiated the front surface of the transparent CHCl shell and caused an increased refection efficiency of the VISAR laser beam. Consequently, relatively dark fringes can be observed from the CHCl shell before the arrival of the main pulse, $t = 0$ ns, in Figure 2(b). When the main pulse arrived, the shock in the CHCl shell became a reflector, and the signal of fringes increased abruptly. After the main pulse, at $t = 0.51$ ns, the VISAR signal disappeared as the shock broke out at the rear surface and released into the vacuum. This indicates a shock velocity of 98 km/s.

For comparison, Figure 2(c) shows the VISAR result for the two-ramp pulse shot, along with the temporal intensities of the VISAR fringes. Before $t = 0$ ns, the relatively bright fringes represent reflections of the VISAR probe laser from the wall at the cone tip and the supporting Al plate (see Target B in Figure 1). Similar to the rectangle pulse case, the weak fringes at the cone hole can be observed by the reflection of the coarse surface of the CHCl shell due to the pre-pulse before the two-ramp pulse. From $t = 0$ ns, the main pulse irradiates the CHCl shell and forms shocks within it, and the fringes reflected from these shocks can be clearly observed. Unlike the rectangle pulse case, the fringes in this two-ramp shot last for 3.1 ns before disappearing. This is because the first ramp pulse is much weaker than the rectangle pulse, resulting in weaker shocks that propagate slower. This ramp compresses the shell close to an isentropic compression. When the first ramp pulse arrives at $t = 0$ ns, the increase in the fringe intensity indicates the formation of a shock reflector. The weak fringe signals caused by the beginning of the first ramp pulse suggest that the initial shocks may still be nearly transparent for the probe laser beam. From 0 to 3.1 ns, the temporal rise in signal intensity suggests that the shocks are getting stronger with time, and thus the reflectivity for the probe laser beam becomes larger[18]. The VISAR blanking observed at around 1.0 ns may be due to either the photoionization of the target material ahead of the shock by the X-rays from the ablation corona[19] or the CHCl material being compressed to a state that turns optically opaque to the probing laser[20]. At 2.5 ns, the second ramp pulse irradiates the target and causes a short discontinuity in the fringes. At 3.1 ns, the sudden increase in fringe signals indicates that the shocks generated by the second ramp pulse overtake the former shocks generated by the first ramp pulse and break out at the rear surface of the CHCl shell, which then causes the fringes to disappear. This agrees with the simulation well (see below) and suggests that the CHCl shell undergoes a quasi-isentropic compression before being accelerated as a whole by the later ramp.

https://doi.org/10.1017/hpl.2024.24 Published online by Cambridge University Press

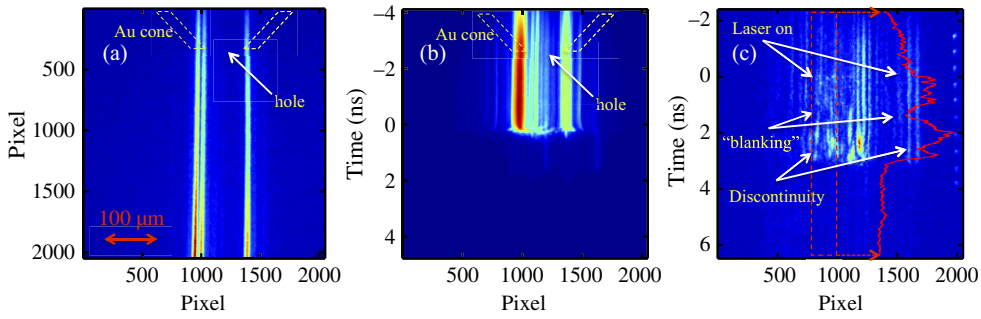


Figure 2. VISAR images for a rectangle pulse and two-ramp pulse shots. (a) The reference image of Target A without the laser shot. (b) The VISAR image for the rectangle pulse shot with Target A. (c) The VISAR image for the two-ramp pulse shot with Target B. The red line represents the temporal intensities of VISAR fringes extracted from the dashed rectangle box.

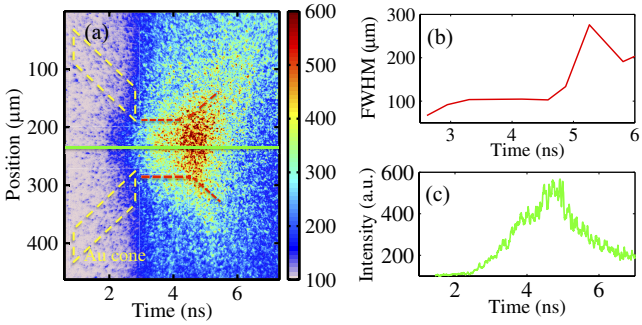


Figure 3. SOP signals of the two-ramp shot. (a) Streaked image of emissions, with an illustration of the gold cone shown to indicate the corresponding locations. (b) Temporal FWHM of the emission source. (c) Lineout along the central axis of the CHCl shell in the SOP image.

Temporal emissions from the shock in the CHCl shell, measured with the SOP, are shown in Figure 3(a), together with an illustration of the gold cone indicating the corresponding spatial locations. The horizontal direction corresponds to the time, increasing from left to right. Initially, the emission is observed to be well collimated. As time increases, the spatial size of the emission increases, and the intensity also strengthens. The full widths at half maximum (FWHMs) of the emission source are plotted in Figure 3(b) as a function of time. The FWHM of the source is 100 ± 5 μm from $t = 2.95$ ns to $t = 4.59$ ns. This is identical to the diameter of the cone tip hole (100 μm), indicating that the plasma is inside the cone. The starting time ($t = 2.95$ ns) for this constant FWHM also serves as a cross-check of the VISAR results for the time when the shocks break out at the rear surface of the shell. A sharp increase in the FWHM can be seen from $t = 4.59$ ns, followed by a quick decrease in less than 1 ns. This is because the SOP records mainly the emissions from the tip cone hole before $t = 4.59$ ns and from the expanding plasmas passing through the cone's tip hole after $t = 4.59$ ns. By combining the expanding spatial distance and the travel time, the expansion speed of the plasmas can be estimated to be 126.8 ± 17.1 km/s. This speed is in agreement with the results from an X-ray pinhole streak camera (XPSC)[21]. A similar jet with a velocity of about 600 km/s was reported[22] at a laser intensity of 700 TW/cm^2.

Emission signals along the central axis of the CHCl shell are extracted and are shown in Figure 3(c). Starting from 1.45 ns, an emission signal appears in the SOP record, albeit at the same level as the background. The steady increase in emission implies a gradual strengthening of the shock over time. This is consistent with the VISAR results, where increased shocks are also observed. Emission signals from the strong shocks generated by the second ramp become clearly distinguishable from 2.5 ns onward. Although these strong shocks have not overtaken those of the first ramp at that time, their emissions can penetrate through the preceding shocks, which are not fully opaque. Rare signals are detected from the shocks generated by the first ramp, suggesting that the compression is along an isentropic path. This self-emission reaches its maximum value at 4.91 ns.

The experimental results are simulated with the 2D cylindrical hydrodynamic code FLASH[23,24], which includes radiation transport, electron thermal conduction, laser energy deposition and the three-temperature model. The simulation results are shown in Figure 4. The laser energy is 5 kJ, with a wavelength of 0.351 μm and a spot radius of 250 μm, the same as the experimental design conditions. In the simulations, the laser propagates along the cone wall and focuses at the top of the CH target. The input parameters are the exact experimental design conditions for the laser and target, with the exception that the simulations employ a CH target due to lack of opacity data for CHCl targets. The MPQEOS equations of state[25] and the SNOP opacity tables[26] are used for the CH target. The target has an inner radius of 250 μm and a thickness of 50 μm, as shown in Figure 4(a).

The simulation results for the rectangle pulse are shown in Figures 4(a) and 4(b). The shock positions are clearly discernible by the steepest gradient density distributions. At $t = 0.589$ ns, the shock reaches the rear surface of the CH shell, indicating that the VISAR signals will soon disappear. This time (0.589 ns) is in good agreement with our experimental results, where the fringes disappear at 0.51 ns,

https://doi.org/10.1017/hpl.2024.24 Published online by Cambridge University Press

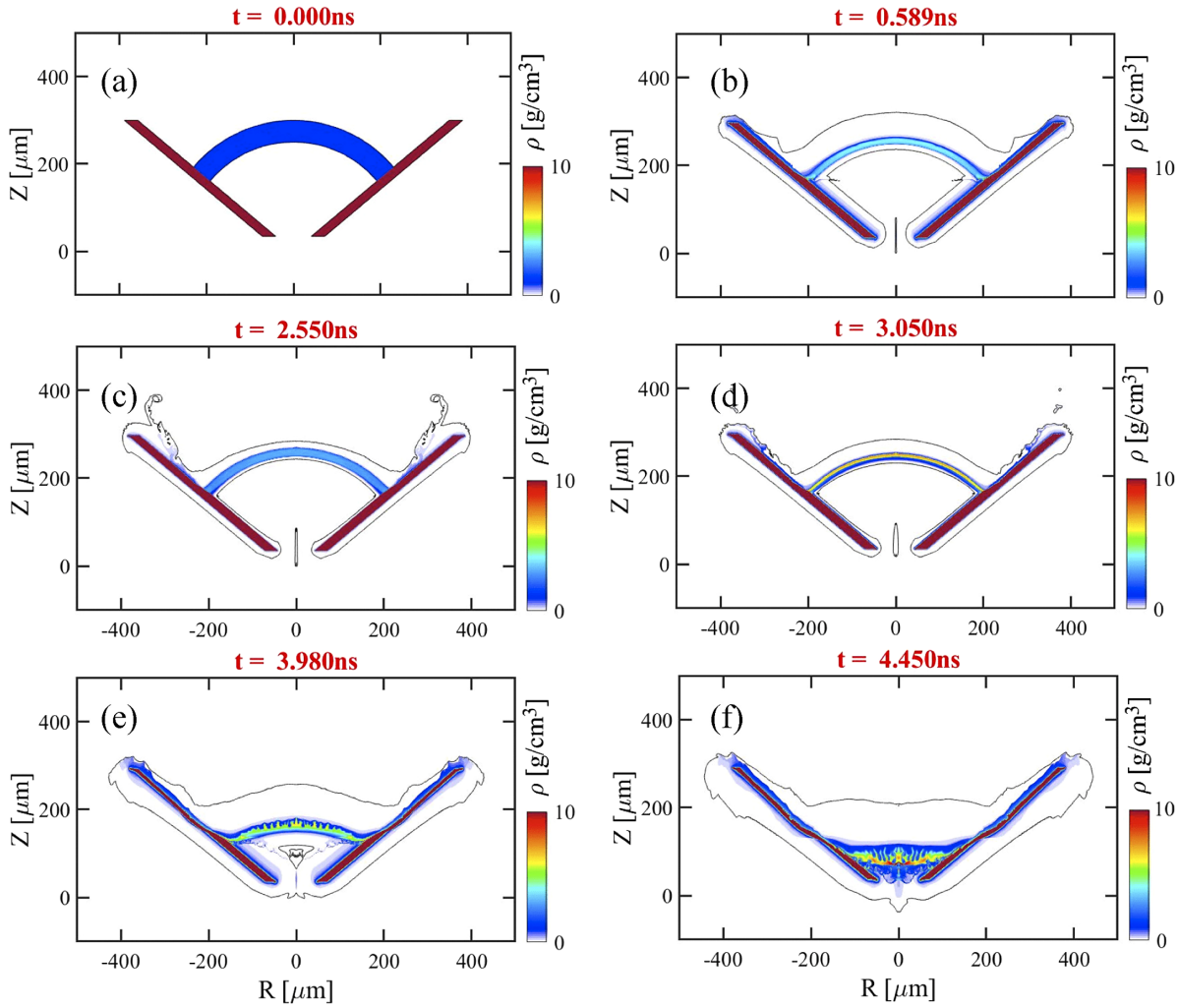


Figure 4. Temporal density distributions in the CHCl shell. (a), (b) Simulation of density distribution in the CHCl shell for rectangle pulse shots at $t = 0$ and $t = 0.589$ ns. (c)–(f) Simulation of density distribution in the CHCl shell for two-ramp pulse shots from $t = 2.550$ ns to $t = 4.450$ ns.

considering the experimental uncertainties (±100 ps). In the simulations of the two-ramp pulse shot, shown in Figures 4(c)–4(f), the first ramp pulse is relatively weak, causing the shock to propagate more slowly in the CH shell compared to the rectangle shot. The first shock reaches the rear surface of the shell at $t = 2.55$ ns (Figure 4(c)), and the strong shocks start to form due to ablation by the second ramp. This corresponds with the records from the SOP, where strong signals are detected starting at $t = 2.5$ ns. These strong shocks break out at the rear surface of the CH shell at 3.05 ns in the simulation (Figure 4(d)), coinciding with experimental measurement by VISAR (3.1 ns). The VISAR record disappears at 3.1 ns, making it impossible to gain information from this optical diagnostic beyond this point. Fortunately, the SOP results continue to provide insights into the evolution of plasma both inside and outside the gold cone. The plasmas begin to emerge from the tip hole of the cone at 4.45 ns and subsequently expand freely, as shown in Figure 4(f). This agrees well with the SOP results, which show a sharp increase in the FWHM of the source size from $t = 4.59$ ns. As we compared above, the time differences between the simulation results and the measurements obtained by the VISAR and SOP are no more than 150 ps. While this value is slightly larger than the experimental errors (±100 ps), it is noteworthy that the experimental laser power is smaller than the designed pulse power. Consequently, it takes more time for the plasmas to emerge from the tip hole in the experiment than in the simulations in which the designed laser shape is used. Considering this respect, we believe that the agreement between the simulations and the experimental measurements is reasonable.

Figure 5 shows the simulated density distributions along the axis of the CH shell targets at different times. From $t = 0$ to $t = 2.55$ ns, the CH shell is compressed by the shocks from the first ramp pulse. As time increases, the CH shell is fully compressed to a density of 3.75 g/cm^3 by the end of the first pulse. Essentially, this process is the same as a typical spherical convergence, where the CH

https://doi.org/10.1017/hpl.2024.24 Published online by Cambridge University Press

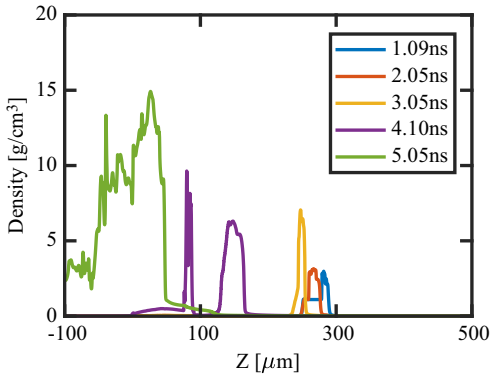


Figure 5. The density along the target axis at different times for the two-ramp pulse shot.

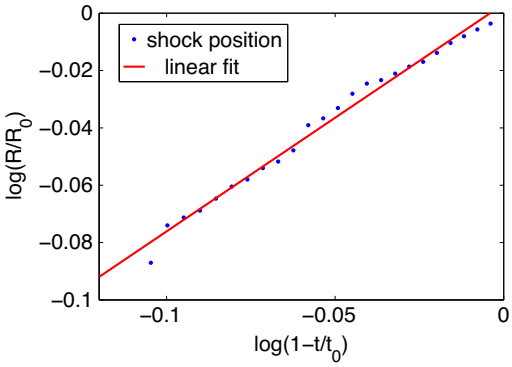


Figure 6. Converging shock positions versus the time in simulations. The blue dots are normalized shock positions and the red line is the linear fit.

shell is compressed by converging shock waves (CSWs). The trajectory of the CSW can be well described by the Chester–Chisnell–Whitham (CCW) method[27]. In the strong shock limit, this method is in a good agreement with the Guderley theory[28]: $\frac{R}{R_0} = \left(1 - \frac{t}{t_0}\right)^n$, where R_0 is the shock initial position, t_0 is the arrival time at the center of the shell and n is the similarity exponent, related to the adiabatic exponent γ. The simulations shown in Figure 6 plot the normalized converging shock positions against the normalized time relative to the arrival time at the shell center in a log–log coordinate system. The slope of the linear fit to this line gives the similarity exponent, $n = 0.798$, in the Guderley formula. In spherical shocks, this similarity exponent corresponds to the adiabatic exponent $\gamma = 1.10$ for ideal gas[29]. Solids with a Grüneisen parameter Γ_0 behave similar to the gas with the adiabatic exponent $\gamma = \Gamma_0 + 1$[30]. Based on this, the Grüneisen parameter was calculated for the CH shell, yielding a value of $\Gamma_0 = 0.10$. This value is less than that in the common reference data[31]. However, recent calculations and experimental measurements on CH or glow discharge polymer (GDP)[32,33] suggest that the Grüneisen parameter is less than 0.2 at low densities, which is in good agreement with our results. The peak density of 3.75 g/cm^3 in our spherical compression by the first ramp is also higher than the density (less than 3.5 g/cm^3) in planar compression[34], indicating that the shock strengthens in the converging process.

After the first ramp, shocks generated by the second ramp uniformly compress this pre-compressed CH shell to a density as high as 7.5 g/cm^3 at 3.05 ns, indicating that these strong shocks reach the rear surface of the CH. Subsequently, the entire CH shell is accelerated forward and simultaneously compressed by the pressure from both the laser ablation and the squeeze from the wall of the gold cone as it moves toward the tip of the cone. This process is 3D. With the drive laser on, the densities of the CH shell remain almost constant (7.5 g/cm^3), while the thickness of the shell increases again since its spherical radius decreases when approaching the tip of the cone, shown in Figure 5 at 4.1 ns. At the end of the drive laser ($t = 4.5$ ns), the central part of the CH shell continues to move at high speed, while the marginal parts move more slowly due to the expansion of the cone wall into the cone, which prevents direct interaction of the laser pulse with the margin of CH shell, and also due to the drag of the inner wall of the gold cone. Consequently, the CH shell becomes flattened, as shown in Figure 4(f). A high-density plasma jet forms due to inertia of the shell. Upon collision between the marginal parts of the CH shell and the cone wall, a recoil force further compresses the jet as it moves toward the cone tip. The highest density of 14.92 g/cm^3 is achieved at $t = 5.05$ ns, represented by the green line in Figure 5. Since the emission is proportional to the density of the plasma, this is also in agreement with the SOP measurements, which show the strongest emission at $t = 4.91$ ns. Thus, we have shown that with the gold cone, a high-density jet with high velocity can be produced. The gold cone plays an important role in containing and compressing the plasma jet before the jet ejects from the tip hole.

4. Summary and conclusions

The CHCl shell in the gold cone was irradiated by a specially designed laser shape, namely the two-ramp pulse. The shocks generated by the first ramp fulfilled the quasi-isentropic compression of the target. Subsequent shocks generated by the second ramp further compressed and accelerated the shell to generate a high-density jet with high velocity. The shock velocity profiles in the CH shell were measured by VISAR, while the emissions from the shocks were recorded by the SOP. The steady increase in the intensity of both the VISAR fringes and the SOP signals indicates that the shocks grew stronger as they propagated through the CH shell. The measured arrival times of shocks at the rear surface of the CH shell are in good agreement with the simulation results conducted by the hydrodynamic code FLASH, considering the experimental inaccuracies (±100 ps). The plasma jet was ejected from the tip hole of the gold cone and

https://doi.org/10.1017/hpl.2024.24 Published online by Cambridge University Press

reached the maximum emission at the predicted times given by the code. In addition, for shots with the rectangle laser pulse, the measured shocks with a velocity of 98 km/s were also well reproduced in the simulation results. This gives us confidence in the simulation results and demonstrates our ability to generate the required jet conditions under current laser conditions. The path through which converging shock transported in the CH shell agrees with Guderley's theory, showing the increasing shock strength. The CH plasma jet, driven by the ablation of the second ramp pulse in the gold cone, can reach a maximum density of 14.92 g/cm^3 according to simulations, with a velocity measured up to 126.8 $\pm$ 17.1 km/s. In conclusion, generation of high-density and high-velocity plasma jets with a two-ramp pulse has been demonstrated experimentally in a preliminary shock experiment for DCI campaigns. The benchmarked code will be modified to optimize the experimental design, and new diagnostics are being developed for subsequent experiments with an upgraded laser system. These well-characterized jets will be used for the next steps of DCI campaigns, where the two jets will collide into each other and be trapped by external magnetic fields to prepare the necessary conditions for fast heating by fast electrons.

Acknowledgement

We thank all the staff of the SGII-U laser facility for the support of the experiment and the staff of the Shanghai Institute of Laser–Plasma and Shanghai Jiao Tong University for the target fabrication. This work was supported by the Strategic Priority Research Program of the Chinese Academy of Sciences (Grant Nos. XDA25030500 and XDA25050200), the National Natural Science Foundation of China (Grant Nos. 11988101, 11890694, 12173058, and 12175309), the National Key R&D Program of China (Grant Nos. 2019YFA0405502 and 2022YFA1603204), and the CAS Youth Interdisciplinary Team (Grant No. JCTD-2022-05).

References

1. J. D. Lindl, Phys. Plasmas **2**, 3933 (1995).
2. S. P. Regan, V. N. Goncharov, I. V. Igumenshchev, T. C. Sangster, R. Betti, A. Bose, T. R. Boehly, M. J. Bonino, E. M. Campbell, D. Cao, T. J. B. Collins, R. S. Craxton, A. K. Davis, J. A. Delettrez, D. H. Edgell, R. Epstein, C. J. Forrest, J. A. Frenje, D. H. Froula, M. G. Johnson, V. Y. Glebov, D. R. Harding, M. Hohenberger, S. X. Hu, D. Jacobs-Perkins, R. Janezic, M. Karasik, R. L. Keck, J. H. Kelly, T. J. Kessler, J. P. Knauer, T. Z. Kosc, S. J. Loucks, J. A. Marozas, F. J. Marshall, R. L. McCrory, P. W. McKenty, D. D. Meyerhofer, D. T. Michel, J. F. Myatt, S. P. Obenschain, R. D. Petrasso, P. B. Radha, B. Rice, M. J. Rosenberg, A. J. Schmitt, M. J. Schmitt, W. Seka, W. T. Shmayda, M. J. Shoup, A. Shvydky, S. Skupsky, A. A. Solodov, C. Stoeckl, W. Theobald, J. Ulreich, M. D. Wittman, K. M. Woo, B. Yaakobi, and J. D. Zuegel, Phys. Rev. Lett. **117**, 025001 (2016).
3. J. D. Lindl, P. Amendt, R. L. Berger, S. G. Glendinning, S. H. Glenzer, S. W. Haan, R. L. Kauffman, O. L. Landen, and L. J. Suter, Phys. Plasmas **11**, 339 (2004).
4. A. B. Zylstra, A. L. Kritcher, O. A. Hurricane, D. A. Callahan, K. Baker, T. Braun, D. T. Casey, D. Clark, K. Clark, T. Döppner, L. Divol, D. E. Hinkel, M. Hohenberger, C. Kong, O. L. Landen, A. Nikroo, A. Pak, P. Patel, J. E. Ralph, N. Rice, R. Tommasini, M. Schoff, M. Stadermann, D. Strozzi, C. Weber, C. Young, C. Wild, R. P. J. Town, and M. J. Edwards, Phys. Rev. Lett. **126**, 025001 (2021).
5. O. A. Hurricane, D. A. Callahan, D. T. Casey, P. M. Celliers, C. Cerjan, E. L. Dewald, T. R. Dittrich, T. Döppner, D. E. Hinkel, L. F. Berzak Hopkins, J. L. Kline, S. Le Pape, T. Ma, A. G. MacPhee, J. L. Milovich, A. Pak, H.-S. Park, P. K. Patel, B. A. Remington, J. D. Salmonson, P. T. Springer, and R. Tommasini, Nature **506**, 343 (2014).
6. R. Betti and O. Hurricane, Nat. Phys. **12**, 435 (2016).
7. R. Betti, C. D. Zhou, K. S. Anderson, L. J. Perkins, W. Theobald, and A. A. Solodov, Phys. Rev. Lett. **98**, 155001 (2007).
8. M. Tabak, J. Hammer, M. E. Glinsky, W. L. Kruer, S. C. Wilks, J. Woodworth, E. M. Campbell, M. D. Perry, and R. J. Mason, Phys. Plasmas **1**, 1626 (1994).
9. S. A. Slutz, M. C. Herrmann, R. A. Vesey, A. B. Sefkow, D. B. Sinars, D. C. Rovang, K. J. Peterson, and M. E. Cuneo, Phys. Plasmas **17**, 056303 (2010).
10. J. Zhang, W. M. Wang, X. H. Yang, D. Wu, Y. Y. Ma, J. L. Jiao, Z. Zhang, F. Y. Wu, X. H. Yuan, Y. T. Li, and J. Q. Zhu, Philos. Trans. R. Soc. A **378**, 20200015 (2020).
11. H. F. Robey, P. M. Celliers, J. L. Kline, A. J. Mackinnon, T. R. Boehly, O. L. Landen, J. H. Eggert, D. Hicks, S. Le Pape, D. R. Farley, M. W. Bowers, K. G. Krauter, D. H. Munro, O. S. Jones, J. L. Milovich, D. Clark, B. K. Spears, R. P. J. Town, S. W. Haan, S. Dixit, M. B. Schneider, E. L. Dewald, K. Widmann, J. D. Moody, T. Döppner, H. B. Radousky, A. Nikroo, J. J. Kroll, A. V. Hamza, J. B. Horner, S. D. Bhandarkar, E. Dzenitis, E. Alger, E. Giraldez, C. Castro, K. Moreno, C. Haynam, K. N. LaFortune, C. Widmayer, M. Shaw, K. Jancaitis, T. Parham, D. M. Holunga, C. F. Walters, B. Haid, T. Malsbury, D. Trummer, K. R. Coffee, B. Burr, L. V. Berzins, C. Choate, S. J. Brereton, S. Azevedo, H. Chandrasekaran, S. Glenzer, J. A. Caggiano, J. P. Knauer, J. A. Frenje, D. T. Casey, M. Gatu Johnson, F. H. Seguin, B. K. Young, M. J. Edwards, B. M. Van Wonterghem, J. Kilkenny, B. J. MacGowan, J. Atherton, J. D. Lindl, D. D. Meyerhofer, and E. Moses, Phys. Rev. Lett. **108**, 215004 (2012).
12. H. F. Robey, T. R. Boehly, P. M. Celliers, J. H. Eggert, D. Hicks, R. F. Smith, R. Collins, M. W. Bowers, K. G. Krauter, P. S. Datte, D. H. Munro, J. L. Milovich, O. S. Jones, P. A. Michel, C. A. Thomas, R. E. Olson, S. Pollaine, R. P. J. Town, S. Haan, D. Callahan, D. Clark, J. Edwards, J. L. Kline, S. Dixit, M. B. Schneider, E. L. Dewald, K. Widmann, J. D. Moody, T. Doppner, H. B. Radousky, A. Throop, D. Kalantar, P. DiNicola, A. Nikroo, J. J. Kroll, A. V. Hamza, J. B. Horner, S. D. Bhandarkar, E. Dzenitis, E. Alger, E. Giraldez, C. Castro, K. Moreno, C. Haynam, K. N. LaFortune, C. Widmayer, M. Shaw, K. Jancaitis, T. Parham, D. M. Holunga, C. F. Walters, B. Haid, E. R. Mapoles, J. Sater, C. R. Gibson, T. Malsbury, J. Fair, D. Trummer, K. R. Coffee, B. Burr, L. V. Berzins, C. Choate, S. J. Brereton, S. Azevedo, H. Chandrasekaran, D. C. Eder, N. D. Masters, A. C. Fisher, P. A. Sterne, B. K. Young, O. L. Landen, B. M. Van Wonterghem, B. J. MacGowan, J. Atherton, J. D. Lindl, D. D. Meyerhofer, and E. Moses, Phys. Plasmas **19**, 042706 (2012).
13. J. Q. Zhu, J. Zhu, X. C. Li, B. Q. Zhu, W. X. Ma, X. Q. Lu, W. Fan, Z. G. Liu, S. L. Zhou, G. Xu, G. W. Zhang, X. L. Xie, L. Yang, J. F. Wang, X. P. Ouyang, L. Wang, D. W. Li, P. Q.

https://doi.org/10.1017/hpl.2024.24 Published online by Cambridge University Press

Yang, Q. T. Fan, M. Y. Sun, C. Liu, D. A. Liu, Y. L. Zhang, H. Tao, M. Z. Sun, P. Zhu, B. Y. Wang, Z. Y. Jiao, L. Ren, D. Z. Liu, X. Jiao, H. B. Huang, and Z. Q. Lin, High Power Laser Sci. Eng. **6**, e55 (2018).
14. G. N. Zheng, T. Tao, Q. Jia, R. Yan and J. Zheng, Plasma Phys. Control. Fusion **64**, 105003 (2022).
15. H. Liu, X. H. Yang, Y. H. Zhang, Y. Fang, Z. Zhang, X. H. Yuan, Y. T. li, and J. Zhang, Phys. Rev. E **105**, L053203 (2022).
16. D. W. Yuan, S. J. Wang, H. G. Wei, H. C. Gu, Y. Dai, J. Y. Zhong, Y. T. Li, G. Zhao, and J. Zhang, High Power Laser Sci. Eng. **12**, e6 (2024).
17. Q. Xiao, X. Pan, J. T. Guo, X. Q. Wang, J. F. Wang, X. Q. Jiang, G. Y. Li, X. H. Lu, X. C. Wang, S. L. Zhou, and X. C. Li, Appl. Opt. **59**, 6070 (2020).
18. M. A. Barrios, D. G. Hicks, T. R. Boehly, D. E. Fratanduono, J. H. Eggert, P. M. Celliers, G. W. Collins, and D. D. Meyerhofer, Phys. Plasmas **17**, 056307 (2010).
19. S. Laffite, S. D. Baton, P. Combis, J. Clerouin, M. Koenig, V. Recoules, C. Rousseaux, and L. Videau, Phys. Plasmas **21**, 082705 (2014).
20. N. J. Hartley, C. Zhang, X. Duan, L. G. Huang, S. Jiang, Y. Li, L. Yang, A. Pelka, Z. Wang, J. Yang, and D. Kraus, Matter Radiat. Extremes **5**, 028401 (2020).
21. Z. Zhang, X. H. Yuan, Y. H. Zhang, H. Liu, K. Fang, C. L. Zhang, Z. D. Liu, X. Zhao, Q. L. Dong, G. Y. Liu, Y. Dai, H. C. Gu, Y. T. Li, J. Zheng, J. Y. Zhong, and J. Zhang, Acta Phys. Sin. **71**, 155201 (2022).
22. H. Azechi, T. Sakaiya, T. Watari, M. Karasik, H. Saito, K. Ohtani, K. Takeda, H. Hosoda, H. Shiraga, M. Nakai, K. Shigemori, S. Fujioka, M. Murakami, H. Nagatomo, T. Johzaki, J. Gardner, D. G. Colombant, J. W. Bates, A. L. Velikovich, Y. Aglitskiy, J. Weaver, S. Obenschain, S. Eliezer, R. Kodama, T. Norimatsu, H. Fujita, K. Mima, and H. Kan, Phys. Rev. Lett. **102**, 235002 (2009).
23. B. A. Fryxell, K. Olson, P. Ricker, F. X. Timmes, M. Zingale, D. Q. Lamb, P. MacNeice, R. Rosner, J. W. Truran, and H. Tufo, Astrophys. J. Suppl. **131**, 273 (2000).
24. A. Dubey, K. Antypas, M. K. Ganapathy, L. B. Reid, K. Riley, D. Sheeler, A. Siegel, and K. Weide, Parallel Comp. **35**, 512 (2009).
25. A. J. Kemp and J. Meyer-ter-Vehn, Nucl. Instrum. Methods Phys. Res. A **415**, 674 (1998).
26. K. Eidmann, Laser Particle Beams **12**, 223 (1994).
27. G. B. Whitham, *Linear and Nonlinear Waves* (Wiley, 1974), p. 263.
28. G. Guderley, Luftfahrtforschung **19**, 302 (1942).
29. L. E. Bilbao and J. Gratton, IL Nuovo Cimento **18**, 9 (1996).
30. Zeldovich and Y. P. Raizer, *Physics of Shock Waves and High Temperature Hydrodynamic Phenomena* (Academic Press, 1966), p. 700.
31. M. A. Meyers, *Dynamic Behavior of Materials* (John Wiley & Sons, Inc., 1994), p. 128.
32. P. Colin-Lalu, V. Recoules, G. Salin, T. Plisson, E. Brambrink, T. Vinci, R. Bolis, and G. Huser, Phys. Rev. E **94**, 023204 (2016).
33. C. A. McCoy, S. X. Hu, M. C. Marshall, D. N. Polsin, D. E. Fratanduono, Y. H. Ding, P. M. Celliers, T. R. Boehly, and D. D. Meyerhofer, Phys. Rev. B **102**, 184102 (2020).
34. S. J. Wang, D. W. Yuan, H. G. Wei, F. Y. Wu, H. C. Gu, Y. Dai, Z. Zhang, X. H. Yuan, Y. T. Li, and J. Zhang, Phys. Plasmas **29**, 112701 (2022).

https://doi.org/10.1017/hpl.2024.24 Published online by Cambridge University Press